


## Perturbative and nonperturbative photoionization of $\text{H}_2$ and $\text{H}_2\text{O}$ using the molecular $R$ -matrix-with-time method

J. Benda<sup>1,2,\*</sup>, J. D. Gorfinkiel<sup>1</sup>, Z. Mašín<sup>2</sup>, G. S. J. Armstrong<sup>3</sup>, A. C. Brown<sup>3</sup>,  
D. D. A. Clarke<sup>3,†</sup>, H. W. van der Hart<sup>3</sup> and J. Wragg<sup>3</sup>

<sup>1</sup>*School of Physical Sciences, The Open University, Milton Keynes MK7 6AA, United Kingdom*

<sup>2</sup>*Institute of Theoretical Physics, Faculty of Mathematics and Physics, Charles University,  
V Holešovičkách 2, Prague 8, 180 00, Czech Republic*

<sup>3</sup>*Centre for Theoretical Atomic, Molecular and Optical Physics, School of Mathematics and Physics,  
Queen's University Belfast, University Road, Belfast BT7 1NN, Northern Ireland, United Kingdom*

 (Received 30 April 2020; accepted 20 October 2020; published 23 November 2020; corrected 25 February 2021)

The *ab initio*  $R$ -matrix with time method has recently been extended to allow simulation of fully nonperturbative multielectron processes in molecules driven by ultrashort arbitrarily polarized strong laser fields. Here we demonstrate the accuracy and capabilities of the current implementation of the method for two targets: We study single-photon and multiphoton ionization of  $\text{H}_2$  and one-photon and strong-field ionization of  $\text{H}_2\text{O}$  and compare the results to available experimental and theoretical data as well as our own time-independent  $R$ -matrix calculations. We obtain a highly accurate description of total and state-to-state single-photon ionization of  $\text{H}_2\text{O}$  and, using a simplified coupled-channel model, we show that state coupling is essential to obtain qualitatively correct results and that its importance as a function of laser intensity changes. We find that electron correlation plays a more important role at low intensities (up to approximately  $50 \text{ TW/cm}^2$ ).

DOI: [10.1103/PhysRevA.102.052826](https://doi.org/10.1103/PhysRevA.102.052826)

### I. INTRODUCTION

Laser technology has been advancing rapidly in the past few decades, providing new tools for probing processes in atoms and molecules with subangstrom spatial and attosecond temporal resolution (see, e.g., Ref. [1]). One of the most sophisticated experimental techniques available is three-dimensional high harmonic spectroscopy [2], recently developed to reconstruct the ionization and recombination steps of strong-field-driven dynamics on the single-molecule level with unprecedented detail. Complementing these measurements with a high-level theoretical description is necessary to understand the multielectron (and nuclear) dynamics that are involved [3–5] and to further our understanding of the behavior and control of laser-driven molecules.

The enormous complexity of modeling dynamics of continuum molecular states embedded in an external field has led to development of several different *ab initio* computational approaches, each with their own strengths and weaknesses, thus providing complementary insights into the problem. This includes the haCC approach [6,7], the  $B$ -spline algebraic diagrammatic construction (ADC) code [8], the Spanner-Patchkovskii method [9], the multiconfigurational strong-field approximation with Gaussian nuclear wave packets approach (MC-SFA-GWP) [10] capable of describing coupled electronic-nuclear dynamics, the recent extension of the Xchem package [11] to calculations of field ionization of small molecules, the time-dependent multiconfiguration

self-consistent-field method based on occupation-restricted multiple-active-space model (TD-ORMAS) [12], the multiconfiguration time-dependent Hartree (MCTDH) method [13,14], time-dependent coupled-cluster (TDCC) method [15–17], the TD close-coupling method [18], and others [19].

Among the methods capable of accurate description of multielectron dynamics in strong fields is the well-established *ab initio*  $R$ -matrix with time-dependence approach (RMT) [20,21]. Until now, RMT has been applied only to processes involving atoms and used to model high harmonic generation [22], to analyze angular distributions of photoelectron momentum in complicated field configurations, including pairs of counterrotating circularly polarized short laser pulses [23,24] and angular streaking [25], and even to processes involving spin-orbit interactions [26]. We note that an alternative implementation of RMT has been applied to  $\text{H}_2^+$  [27].

Recently, we have extended the RMT code to enable molecular calculations [28]. In this paper, we present applications of the method to several simple processes involving small molecules in laser fields of various parameters. Following the standard  $R$ -matrix approach [29], the physical space is divided into an inner and an outer region. In the inner region, RMT represents the time-dependent electronic wave function as a linear combination of field-free time-independent multielectron eigenstates, while in the outer-region standard one-electron channels sampled on a uniformly spaced finite-difference grid are used.

The extension of RMT to molecules is based on the use of the time-independent (stationary) fixed-nuclei molecular  $R$ -matrix package UKRmol+ [30], which provides the eigenstates for the inner region as well as all other time-independent

\*Corresponding author: [jakub.benda@seznam.cz](mailto:jakub.benda@seznam.cz)

†Present address: School of Physics and CRANN Institute, Trinity College Dublin, Dublin 2, Ireland.

molecular input data required by RMT. The RMT code is then responsible for the time evolution of the molecular wave function.

A key feature of the UKRmol+ codes is the flexibility in the description of electron correlation and polarization including the possibility to perform electronically inelastic calculations. Over the years a number of detailed studies have been performed with UKRmol [31] and UKRmol+ on identifying accurate  $R$ -matrix models to use in electron collisions with small to large molecules [32,33] and recently in photoionization of small molecules [3,34–37] and substituted benzenes [38].

However, with the move to time-dependent multiphoton and nonperturbative dynamics using RMT, the field-free scattering models must be tested and modified, where necessary, so as to enable different insights into multielectron dynamics of molecules in external fields. One of the aims of this initial application of the molecular RMT approach is to establish the models required in UKRmol+ to generate molecular data of sufficient quality and study how the RMT results depend on the level of description used.

For the photoionization processes studied in this work, it is also possible to determine cross sections and other quantities like the asymmetry parameter from the stationary approach using UKRmol+; these results are also reported here. As we will see, the results set an upper bound on the quality of their time-dependent counterparts.

In addition, the unique combination of capabilities of the stationary and time-dependent  $R$ -matrix approaches allows us to use them both to perform photoionization calculations in the perturbative regime on the same level of quality with regard to the description of molecular structure and electron correlation. This allows us to compare the stationary and RMT results and study the field-induced effects in detail.

The paper is organized as follows. In the next section we summarize the theoretical approach. In Secs. III and IV we present the calculations performed using RMT for  $H_2$  and  $H_2O$ , respectively, and describe their characteristics. In Sec. V we summarize the results obtained so far and highlight future applications of the method to molecules.

## II. THEORETICAL APPROACH

The molecular RMT calculations are performed within the fixed-nuclei approximation; this assumes that photoionization processes occur on sufficiently short timescales such that the nuclei can be considered fixed in space. The internal coordinates used in the calculations are normally those of the ground-state equilibrium geometry of the target molecule, whereas its orientation with respect to the field can be selected. The approach can be applied both to neutral targets (when the residual  $N$ -electron system is charged) or to charged targets (when the residual  $N$ -electron system can be neutral or charged). However, for the sake of simplicity, we assume from now on that the residual molecule is an ion.

While the main strength of RMT is the accurate description of correlated multielectron dynamics in strong fields, the method is also applicable to simpler problems of single-photon and multiphoton ionization. We have chosen the study of these processes to test the validity of the approach and assess the quality of the results that can be obtained.

As already stated, the method is based on the separation of space into the inner and outer regions. These are divided by a sphere of radius  $a$ . A small overlap, in the form of a spherical shell of thickness  $\delta$ , between the inner and outer regions is needed to ensure continuity of the wave function between the regions. The effect of the laser field is described within the dipole approximation. The choice of the radius  $a$  should be such that the  $R$ -matrix sphere (without the overlapping spherical shell) fully contains the charge density of the residual ( $N$ -electron) states included. In the following we denote by  $\mathbf{X}_{N+1}$  ( $\mathbf{X}_N$ ) all spin-space coordinates of the  $N+1$  ( $N$ ) electrons.

In the inner region,  $r \leq a$ , the full electron-electron and electron-laser interaction is considered and the time-dependent Schrödinger equation for  $N+1$  electrons is solved

$$i \frac{\partial}{\partial t} \Psi(\mathbf{X}_{N+1}, t) = H(t) \Psi(\mathbf{X}_{N+1}, t), \quad (1)$$

$$H(t) = H_{N+1} + D_{N+1}(t). \quad (2)$$

Here  $H_{N+1}$  is the nonrelativistic fixed-nuclei Hamiltonian of the molecule and  $D_{N+1}$  describes the time-dependent electric field  $\mathbf{E}(t)$  in the length gauge and dipole approximation

$$H_{N+1} = \sum_{i=1}^{N+1} \left( -\frac{1}{2} \nabla_i^2 + \sum_{i>j}^{N+1} \frac{1}{|\mathbf{r}_i - \mathbf{r}_j|} - \sum_{k=1}^{nuclei} \frac{Z_k}{|\mathbf{r}_i - \mathbf{R}_k|} \right), \quad (3)$$

$$D_{N+1} = \mathbf{E}(t) \cdot \sum_{i=1}^{N+1} \mathbf{r}_i, \quad (4)$$

where  $R_k$  and  $Z_k$  are the positions of the nuclei and their charges, respectively. The time-dependent wave function  $\Psi(\mathbf{X}_{N+1}, t)$  of the whole ( $N+1$ )-electron system is expressed as a linear combination of time-independent eigenstates  $\psi_k(\mathbf{X}_{N+1})$ ,

$$\Psi(\mathbf{X}_{N+1}, t) = \sum_k C_k(t) \psi_k(\mathbf{X}_{N+1}), \quad (5)$$

$$(H_{N+1} + L_{N+1}) \psi_k(\mathbf{X}_{N+1}) = E_k \psi_k(\mathbf{X}_{N+1}), \quad (6)$$

where the wave functions  $\psi_k(\mathbf{X}_{N+1})$ , restricted to the inner region, contain a continuum contribution (discussed below) and do not vanish on the boundary  $r = a$  between the inner and the outer region. Hermiticity of the inner-region Hamiltonian in this basis is ensured by including the Bloch operator  $L_{N+1}$  [20,29] acting only at the boundary.

With the help of the Bloch operator, the full Hamiltonian  $H(t)$  is rewritten in the form

$$H(t) = H_I(t) - L_{N+1}, \quad (7)$$

$$H_I(t) = (H_{N+1} + L_{N+1}) + D_{N+1}, \quad (8)$$

where  $(H_{N+1} + L_{N+1})$  is now Hermitian. Inserting the expansion (5) into the Schrödinger equation (1) and projecting it on the inner-region basis  $\psi_k(\mathbf{X}_{N+1})$ , we obtain a system of equations for the expansion coefficients  $C_k(t)$ ,

$$i \frac{d}{dt} \mathbf{C}(t) = \mathbf{H}_I(t) \mathbf{C}(t) - \mathbf{S}(t), \quad (9)$$

$$\begin{aligned}
H_{I,k'k}(t) &= \langle \psi_{k'} | H_{N+1} + L_{N+1} + \mathbf{E}(t) \cdot \sum_{i=1}^{N+1} \mathbf{r}_i | \psi_k \rangle \\
&= \delta_{k',k} E_k - \mathbf{E}(t) \cdot \sum_k \mathbf{d}_{k'k}, \quad (10)
\end{aligned}$$

$$S_{k'}(t) = \langle \psi_{k'} | L_{N+1} | \Psi(t) \rangle, \quad (11)$$

where  $E_k$  is the eigenenergy of state  $\psi_k(\mathbf{X}_{N+1})$ ,  $S_{k'}(t)$  are surface terms connecting the inner and outer regions, and  $\mathbf{d}_{k'k}$  is the transition dipole moment vector in Cartesian basis

$$\mathbf{d}_{k'k} = -e \langle \psi_{k'} | \sum_{i=1}^{N+1} \mathbf{r}_i | \psi_k \rangle, \quad (12)$$

$$\mathbf{r}_i = (x_i, y_i, z_i). \quad (13)$$

The time evolution is implemented using an accurate high-order Arnoldi method [20].

In the outer region,  $r \geq a - \delta$ , the exchange interaction between the unbound electron and the residual molecule can be safely neglected. Therefore, the wave function can be expanded in terms of direct products of a residual  $N$ -electron wave function and a continuum function represented on a finite-difference grid

$$\Psi(\mathbf{X}_{N+1}, t) = \sum_p \bar{\phi}_p^{\Gamma_p}(\mathbf{X}_N; \hat{\mathbf{r}}_{N+1} \sigma_{N+1}) \frac{1}{r} f_p(r, t), \quad (14)$$

where the channel wave functions  $\bar{\phi}_p^{\Gamma_p}$  are defined as the residual  $N$ -electron state coupled to the real spherical harmonic  $X_{l_p, m_p}(\hat{\mathbf{r}}_{N+1})$  and spin  $\sigma_{N+1}$  of the continuum electron in the outer region. They are indexed with the collective index  $p = \{i_p, l_p, m_p\}$  denoting the index of the residual state,  $i_p$ , and the angular parts of the unbound electron coupled to it. Finally,  $f_p(r, t)$  is the time-dependent reduced radial wave function of the outer-region electron in channel  $p$  and  $r \equiv r_{N+1}$ . Each combination of a residual state and a channel spherical harmonic transforms as an irreducible representation  $\Gamma_p$  of the molecular point group. The expansion (14) implies that only single ionization is currently possible in RMT. As stated, the continuity between the inner region and the outer region is maintained by an overlapping shell with thickness  $\delta$  of a few atomic units. This overlap allows us to use Eq. (14) to evaluate the surface terms  $S_{k'}(t)$  from Eq. (11),

$$S_{k'}(t) = \frac{1}{2} \sum_p \omega_{pk'} \left. \frac{\partial f_p(r, t)}{\partial r} \right|_{r=a}, \quad (15)$$

where  $\omega_{pk'}$  are amplitudes of the inner-region wave function  $\psi_{k'}(\mathbf{X}_{N+1})$  on the boundary projected on the channel functions  $p$ . The radial derivative is evaluated using a finite-difference approximation straddling the boundary [20].

The time-dependent Schrödinger equation for the outer region is [20,28]

$$i \frac{d}{dt} f_p(r, t) = h_p(r) f_p(r, t) + \sum_{p'} V_{pp'} f_{p'}(r, t), \quad (16)$$

$$h_p(r) = -\frac{1}{2} \frac{d^2}{dr^2} + \frac{l_p(l_p + 1)}{2r^2} - \frac{Z - N}{r} + E_p, \quad (17)$$

where  $h_p$  is a one-electron operator that includes the channel energy  $E_p$ , the screened Coulomb interaction, and the cen-

trifugal barrier. The operator with matrix elements  $V_{pp'}$  can be written as

$$V = W^E + W^D + W^P. \quad (18)$$

Here  $W^E$  is the long-range multipole coupling between channels,  $W^D$  is the laser interaction with the residual ion, and  $W^P$  is that of the laser with the ionized electron (the formulas for the individual terms of  $V$  are given in [28]). No absorbing boundaries are used in this method (although this would in principle be possible), so the outer grid needs to be sufficiently large to prevent reflections of the ionized wave packets from the end point. RMT supports arbitrary electric fields  $\mathbf{E}(t)$ , in terms of both time dependence and polarization orientation, which allows its application to a wide range of ultrafast strong-field phenomena (e.g., high harmonic generation) but also to simple pseudostationary ionization.

As explained above, the UKRmol+ suite is used to generate the eigenstates of the field-free molecular Hamiltonian of the (final)  $N$ -electron and  $(N + 1)$ -electron states of the system. The  $(N + 1)$ -electron eigenstates are expressed in terms of continuum configurations  $\mathcal{A}\Phi_i^N \eta_{ij}$  and  $L^2$  configurations  $\chi_m^{N+1}$  as

$$\begin{aligned}
\psi_k &= \mathcal{A} \sum_{i,j} c_{ijk} \Phi_i^N(\mathbf{X}_N) \eta_{ij}(\mathbf{r}_{N+1} \sigma_{N+1}) \\
&\quad + \sum_m b_{mk} \chi_m^{N+1}(\mathbf{X}_{N+1}), \quad (19)
\end{aligned}$$

where  $\mathcal{A}$  indicates the antisymmetrization operation,  $\eta_{ij}(\mathbf{r}_{N+1} \sigma_{N+1})$  are continuum spin-orbitals dependent on the position vector  $\mathbf{r}_{N+1}$  and spin  $\sigma_{N+1}$  with a nonzero amplitude on the  $R$ -matrix sphere (discussed below),  $\chi_m^{N+1}$  are configurations not containing continuum orbitals, and the coefficients  $c_{ijk}$  and  $b_{mk}$  are obtained by diagonalizing the Hamiltonian using Eq. (6). The summation over  $i$  runs over the subset of all residual ion eigenstates included in the model;  $j$  runs over those continuum orbitals that are coupled by symmetry to the respective residual ion states and that over  $m$  involves configurations generated from the molecular orbitals fully contained inside the inner region.

Implicit in Eq. (19) is the assumption that the correct space-spin coupling of the individual configurations is used to ensure that the resulting wave functions are eigenstates of the total spin and transform as irreducible representations of an Abelian subgroup of the  $D_{2h}$  point group.

The residual ion states  $\Phi_i^N$  and the  $L^2$  configurations  $\chi_m^{N+1}$  are generated using a configuration-interaction approach. The selection of the configurations to include in both terms is very flexible, independent of each other, and ranges from a single-configuration model (i.e., Hartree-Fock model) to the complete-active-space and full configuration-interaction models. Significant work has been done over several years to define the best possible models to use in electron scattering calculations. A detailed description of the different models and their capabilities can be found in [30].

The orbitals used to generate the configurations in the above expansions are of two types: (i) molecular orbitals generated from a set of standard atom-centered Gaussian orbitals (GTOs) fully contained in the inner region and (ii) continuum orbitals  $\eta$  represented by center-of-mass-centered

GTOs and/or  $B$ -spline-type orbitals. (The requirement for all orbitals used in the UKRmol+ calculation to be orthogonal means that the continuum orbitals will also have a contribution from the atom-centered GTOs.) We use external software (usually MOLPRO [39]) to generate the molecular orbitals, which allows us to employ different approximations (self-consistent-field Hartree-Fock, complete active space self-consistent-field (CASSCF), etc.) and investigate their effect. The choice of basis set and orbital model is guided by the need to describe accurately both the ground state of the initial (neutral) molecule and the residual ionic states energetically accessible in the photon energy range of interest.

The transition dipole moments between eigenstates of the  $(N + 1)$ -electron system (12) obtained from UKRmol+ are used in both the stationary and the time-dependent photoionization calculation. In the time-dependent calculation using RMT, transition dipole moments between all pairs  $(k, k')$  of inner-region states are required. Other quantities generated by UKRmol+ and required by RMT include the coefficients that define the long-range potentials in Eq. (18) and the amplitudes  $\omega_{pk}$  of wave functions  $\psi_k$  at several radii smaller than  $a$  inside the overlapping spherical shell [see Eq. (11)]; more details of how these are generated and used can be found in [28,30].

In the time-independent (i.e., stationary) calculation the transition dipoles from Eq. (12) for only a *single*,  $k = i$ , initial state are required and computed. The inner-region transition dipoles can be used to compute channel-resolved partial-wave dipoles and related to perturbative cross sections and corresponding photoelectron angular distribution parameters [34].

### III. PHOTOIONIZATION OF $H_2$

The well-studied hydrogen molecule is an obvious test for a new method (see Ref. [40] and references therein). In particular, multiphoton ionization was investigated by various time-independent methods [41–44]. A comparison of two- and four-photon ionization cross sections between RMT and  $R$ -matrix Floquet approach [41] was performed [28] for a very simplified model of  $H_2$  involving just two bound molecular orbitals and considering a single cation state. Here we provide results obtained with a more sophisticated description of the electronic properties of  $H_2$ .

#### A. Characteristics of the calculation

As stated, the time-independent input data, including the transition dipole moments between eigenstates of both the neutral and singly ionized molecule, needed by RMT were obtained using the UKRmol+ package [30]. The same models were used to determine the cross sections using the second-order perturbation method and for the time-dependent (RMT) results.

In these calculations we used two different atom-centered GTO bases, aug-cc-pVDZ (further abbreviated as ADZ) and aug-cc-pVTZ (abbreviated as ATZ), to describe the stationary electronic states of  $H_2$  and  $H_2^+$ . In both cases we generated all the  $H_2^+$  states resulting from single occupation of one of the bound orbitals of the cation; this led to the inclusion of 18 and 46 ionic states in the calculation, respectively. Since all generated orbitals were used, the  $L^2$  functions included in

the expansion of the wave function of the  $(N + 1)$ -electron system corresponded to a full configuration interaction. The molecular orbitals were obtained using the restricted open-shell Hartree-Fock (ROHF) option in PSI4 [45].

The atomic bases were supplemented with a continuum basis for partial wave angular momenta up to  $\ell = 6$ , centered on the center of mass of the molecule. For ADZ, the basis consisted of 30  $B$ -splines of order 6 spanning the distance from the origin to the  $R$ -matrix radius  $a = 20$  a.u. This radius was sufficient to contain the electronic density of the molecular orbitals and provided a sufficient margin for the inner-region–outer-region overlap. For ATZ, the  $R$ -matrix radius needed to be increased to 30 a.u. to contain the electronic density. We used the same number of  $B$ -splines, as it proved to be sufficient, at the energies considered, even for the larger radius. Some test calculations were performed with partial waves up to  $\ell = 7$  as well as (separately) with radius  $a = 100$  a.u. to make sure that the above-mentioned parameters were sufficient for converged results.

The resulting Hamiltonian matrices for each irreducible representation in the inner region had the rank of about 3500 for ADZ and 9000 for ATZ. In the time-dependent calculation, only the open channels, associated with the ground state of  $H_2^+$ , were included in the wave function of the outer region. This avoided unnecessary solutions for channels never receiving any electronic population. After the reduction, there were at most ten channels for each of the eight irreducible representations; note that the  $D_{2h}$  point group was used in these calculations.

In our calculations, the ionizing pulse was linearly polarized, parallel to the internuclear axis. The field intensity was  $I = 10^9$  W/cm<sup>2</sup>, i.e., weak enough to avoid nonperturbative effects. The profile of the time-dependent electric field consisted of a 30-cycle ramp-on of  $\sin^2$  shape, followed by a long uniform monochromatic part. In another set of calculations we used a 300-cycle ramp-on instead to investigate the effect of this parameter. The generalized  $n$ -photon ionization cross section (in units  $\text{area}^n \times \text{time}^{-n-1}$ ) can be calculated from

$$\sigma^{(n)}(\omega) = \kappa \omega^n / I^n, \quad (20)$$

where  $\omega$  is the energy of a single photon and  $\kappa$  the photoionization rate.

The total time of simulation was 2000 a.u. (48.4 fs) for the 30-cycle ramp-on and 5000 a.u. (120.9 fs) for the 300-cycle ramp-on, to allow the system to enter a quasistationary regime with a well-defined constant  $\kappa$ , resulting typically in a computational time of several tens of thousands of core hours per single-photon energy. The time needed for preparation of the structural data in UKRmol+ was much shorter, with the majority (around 80 core hours for ATZ) spent in the integral calculation.

#### B. Two-photon ionization

The stationary two-photon cross sections from state  $i$  to channel  $p$  for ionization by component  $c$  of the field can be expressed directly in terms of the inner-region dipoles

$$\sigma_{c,pi}^{(2)}(\omega) = 2\pi(2\pi\alpha\omega)^2 \left| \sum_{mn} A_{pm}^{(-)}(E_{pi}) \frac{d_{c,mn}d_{c,ni}}{E_i + \omega - E_n} \right|^2, \quad (21)$$

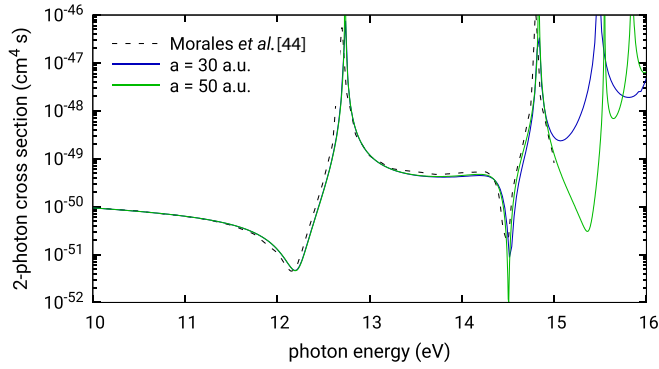


FIG. 1. Cross sections for two-photon ionization of  $H_2$  by a laser field polarized along the molecular axis, calculated from the time-independent perturbation formula (21) for the ATZ model. The calculations differ by the size of the inner region while maintaining the same radial density of the  $B$ -spline continuum basis functions. The results for  $a = 30$  a.u. are sufficiently converged for photon energies up to the second resonance. For convergence at higher photon energies, the size of the inner region would need to be extended.

where  $\alpha$  is the fine-structure constant and the wave-function coefficients  $A_{pm}^{(-)}(E_{pi})$  are used to combine the inner energy-independent eigenstates  $\psi_n$  into a specific channel solution with a given energy and the correct photoionization boundary condition [34]. The kinetic energy of the ejected photoelectron is given by  $E_{pi} = 2\omega - V^{ion}$ , where  $V^{ion}$  is the vertical ionization threshold of channel  $p$  from the initial state  $i$ .

In Eq. (21) we used the approximation

$$\begin{aligned} \frac{1}{E_i + \omega - H_{N+1}} &\simeq \frac{1}{E_i + \omega - H_{N+1} - L_{N+1}} \\ &= \sum_n |\psi_n\rangle \frac{1}{E_i + \omega - E_n} \langle \psi_n|, \end{aligned} \quad (22)$$

valid for photon energies  $\omega$  below the single-photon ionization threshold. That is, instead of using the physical Hamiltonian  $H_{N+1}$  in the Green's operator in Eq. (21) we employed the modified Hamiltonian that includes the Bloch operator, resulting in the Green's-function expansion in terms of the eigenstates  $\psi_n$  [Eq. (19)] and eigenenergies  $E_n$  introduced earlier. This is possible because during the two-photon ionization, at energies below the single-photon ionization threshold, the first photon only excites the target, producing a bound intermediate state. Since bound-state wave functions do not reach the inner-region boundary, the action of the Bloch operator on the bound intermediate state gives zero. This way, though, the size of the inner region puts a constraint on the accurate description of the highly excited states of the neutral molecule whose tail is represented largely by the continuum orbitals  $\eta$  entering Eq. (19). In the following study we restrict ourselves to sufficiently low energies where only the lowest two bound states  $1^1\Sigma_u^+$  and  $2^1\Sigma_u^+$  affect the cross sections. For this setup, in the ATZ model, the inner-region radius  $a = 30$  a.u. is sufficient, as can be seen from Fig. 1. (One can see, however, that just above the second resonance, the results for radius  $a = 50$  a.u. seem to be in better agreement with those of Morales *et al.* [44].)

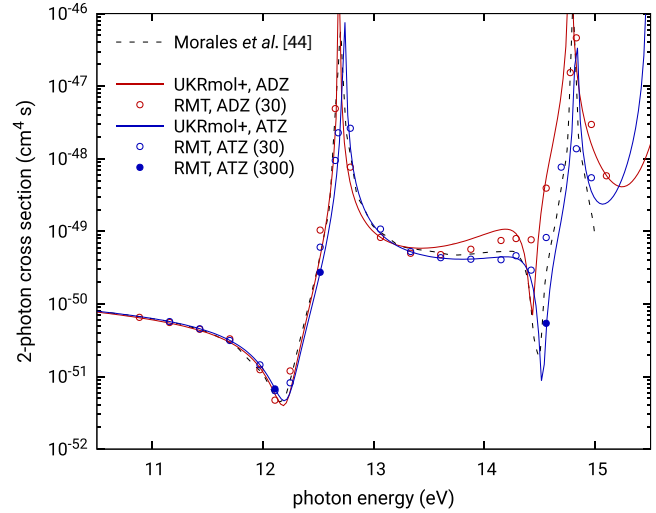


FIG. 2. Two-photon ionization of  $H_2$  by a laser field polarized along the molecular axis, around the resonances corresponding to neutral excited states  $1^1\Sigma_u^+$  and  $2^1\Sigma_u^+$ . Both our time-dependent (circles) and time-independent (lines) results are presented for two different basis sets; for the former and the ATZ basis set, two different turn-on intervals (of 30 and 300 cycles) were used. The theoretical positions of the resonances are given in Table I.

Figure 2 shows the total two-photon ionization cross sections obtained from a linear fit of the time-dependent increase of the outer-region population as calculated by RMT with UKRmol+ input generated using both basis sets. These are compared to the stationary results obtained with UKRmol+ using Eq. (21) and to a two-electron calculation of Morales *et al.* [44], where the photoelectron wave functions were obtained by solving the Schrödinger equation on a discrete variable representation (DVR) grid with the exterior complex scaling boundary condition. The general agreement of all cross sections is very good, with differences increasing in the region of the second resonance. Given the very different numerical methods used in RMT and the calculation of Morales *et al.*, the agreement seen here clearly demonstrates the reliability of our approach.

An aspect that needs to be addressed when using RMT for comparison against results obtained from monochromatic calculations is the bandwidth of the finite-length pulse; RMT is fully time dependent and the laser pulse has only a given number of cycles. To reproduce results from the perturbation method and similar ones, the pulse must be very long and the turn-on of the field very slow to achieve a sufficiently narrow spectrum. In Fig. 2 the RMT cross sections shown were obtained for very long pulses (greater than 100 cycles); for the ATZ basis set we tested the use of a 30-cycle (open blue circles) and a 300-cycle turn-on (closed blue circles, calculated for a subset of photon energies). As can be seen in the figure, in the close vicinity of resonances, a 300-cycle turn-on of the field must be used to obtain agreement with the time-independent results.

The figure also shows the strong improvement of description of the second resonance ( $2^1\Sigma_u^+$ ) when moving from the ADZ model to the better ATZ basis. The results obtained with the latter are barely distinguishable from those of Morales

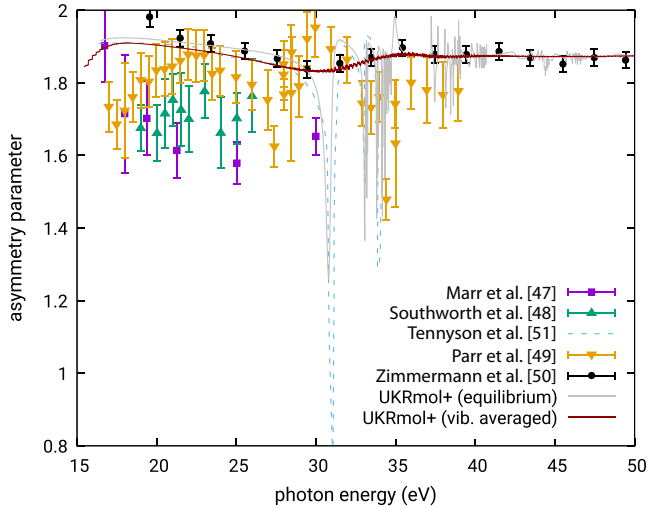


FIG. 3. Fixed-nuclei (equilibrium) and vibrationally averaged effective dipole asymmetry parameter  $\beta_2$  for one-photon ionization of  $\text{H}_2$  compared with experiments of Marr *et al.* [47], Southworth *et al.* [48], Parr *et al.* [49], and Zimmermann *et al.* [50] and an earlier stationary  $R$ -matrix calculation by Tennyson *et al.* [51] with a different molecular model.

*et al.* [44]. These calculations demonstrate the ability of the RMT approach and software to accurately model multiphoton induced processes in molecules, but show the need for a careful tailoring of the pulse and the use of good-quality basis sets. As a further test of the quality of our time-independent calculations, we have calculated the dipole asymmetry parameter  $\beta_2$  of the photoelectron angular distribution for one-photon ionization; see [30] for the exact definition.

Figure 3 shows our results, determined with the ADZ basis set and related input parameters, compared with experimental values and earlier calculations. We chose ADZ over ATZ due to its lower computational requirements, which were particularly significant for the many-geometry calculations discussed below. Still, the agreement is very good, particularly with the experimental data from Ref. [50], except for the 30–35 eV region, where some resonant peaks are clearly visible in the fixed-nuclei (equilibrium geometry) results.

For selected observables and energies, vibrational motion does not necessarily alter the investigated physics. However, this is not the case for  $\beta_2$ . We demonstrate the effect of the vibrational motion in Fig. 3, in which the vibrationally averaged  $\beta_2$  is also shown. The asymmetry parameter was calculated for all final residual vibronic levels from vibrationally resolved partial-wave dipole moments and finally averaged over the vibronic levels using the partial cross sections as weights. The

TABLE I. Vertical excitation thresholds corresponding to the two resonances in Fig. 2, calculated in UKRmol+. Accurate results by Nakashima and Nakatsuji [46] are also listed.

Intermediate state	ADZ	ATZ	Ref. [46]
$1(B)^1\Sigma_u^+$	12.69 eV	12.73 eV	12.75 eV
$2(B')^1\Sigma_u^+$	14.77 eV	14.83 eV	14.85 eV

vibrational states themselves were obtained as eigenstates of the nuclear Hamiltonian on the potential curves of the ground state of the neutral and ionized hydrogen molecule calculated using the multiconfiguration self-consistent-field method with the basis aug-cc-pV5Z in PSI4 [45]. The disappearance of the resonances is obvious in the figure, and small differences in the size of the asymmetry parameter can be seen below 27 eV; the spread of the experimental results prevents us from ascertaining which results agree best with them. In any case, in the present form, RMT does not allow for vibrational motion to be taken into account.

#### IV. PHOTOIONIZATION OF $\text{H}_2\text{O}$

The main strength of the molecular extension of RMT is its direct applicability to arbitrary polyatomic molecules, limited only by the  $R$ -matrix radius and computational resources. We illustrate this feature on photoionization of the water molecule. We note that other, complementary, approaches exist which can treat *ab initio* photoionization of molecules of similar [52] or larger size [53].

Time-dependent calculations for  $\text{H}_2\text{O}$  were performed in the single-active-electron approximation [54,55], strong-field approximation [56], recently using a time-dependent configuration-interaction singles approach [57], and the coupled-cluster method [17]; time-independent calculations have been performed using several approaches [58–60] including a recent GTO-only  $R$ -matrix one [61].

In this section we present photoionization cross sections calculated by the RMT approach, as well as polarization-direction-dependent ionization yields associated with several final cation states after irradiation of the molecule by a short, strong laser pulse. For the former, we have performed high-quality calculations; their characteristics are described in the next section. In the case of the ionization yields, we have employed much simpler models described in Sec. IV C.

##### A. Characteristics of the calculation

For the water molecule we employed the cc-pVTZ basis set and generated ROHF orbitals of the molecular ion  $\text{H}_2\text{O}^+$  in PSI4 [45]. Tests with the aug-cc-pVTZ basis set showed only a small effect on the results. To generate the residual ion wave functions, two complete-active-space models were used: The larger active space was used for a benchmark stationary calculation only, while the smaller active space was used for both the time-dependent and time-independent calculations. In both active spaces two electrons were kept frozen in the lowest-energy orbital (leaving seven active); in the smaller model the next five orbitals (in energy order) were included in the active space, whereas in the larger 14 orbitals were used in the active space. These active spaces can be summarized as (7,5) and (7,14), respectively.

We chose an  $R$ -matrix radius  $a = 15$  a.u., partial waves up to  $\ell = 6$  (although  $\ell = 4$  is sufficient to obtain converged single-photon results), and a purely  $B$ -spline continuum consisting of 30  $B$ -splines of order 6. In the expansion of the  $N + 1$  electronic wave function according to Eq. (19), we included the 50 lowest-lying ionic states of the residual ion in the larger model for a good flexible description in the inner

TABLE II. Vertical ionization potentials for the large (L) and smaller (S) benchmark calculations of photoionization of  $\text{H}_2\text{O}$ . Earlier experimental values of Potts and Price [62] and Brundle *et al.* [64] are also listed.

Final state	$V^{ion}$ (S)	$V^{ion}$ (L)	Ref. [64]	Ref. [62]
$X\ 1^2B_1$	12.20 eV	12.82 eV	12.61 eV	12.6 eV
$A\ 1^2A_1$	14.74 eV	15.18 eV	14.74 eV	14.7 eV
$B\ 1^2B_2$	19.04 eV	19.35 eV	18.55 eV	18.5 eV

region but only four states in the smaller model. Altogether, this leads to a continuum-contracted Hamiltonian of rank around 80 000 for the large model and 1500 for the small model, per each of the four irreducible representations of the  $C_{2v}$  point group to which the molecule belongs. The resulting calculated vertical ionization potentials for the lowest three states of  $\text{H}_2\text{O}^+$  are listed in Table II. For the purpose of Figs. 4 and 5, the ground state in the larger calculation was shifted to recover the experimental first ionization potential (12.6 eV [62]) when determining the cross section.

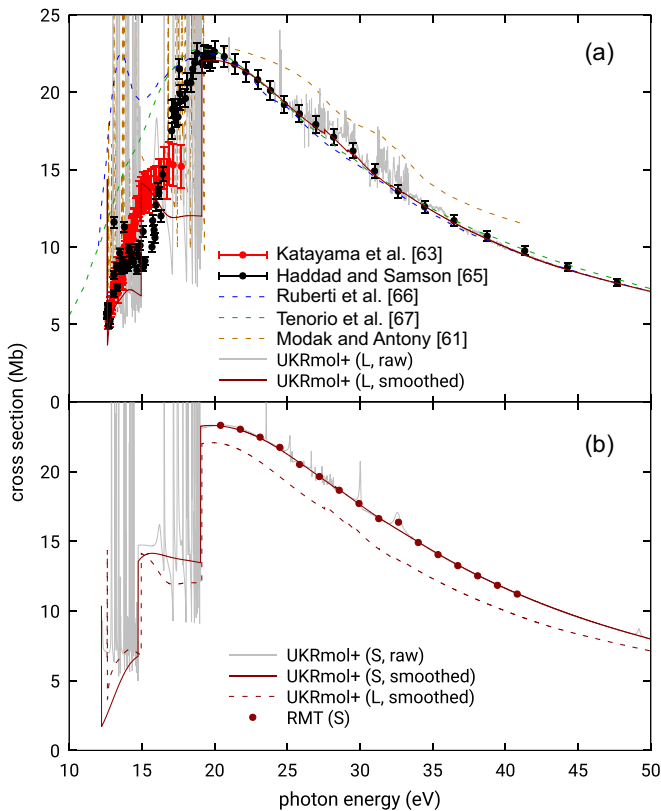


FIG. 4. Orientation-averaged cross section for one-photon ionization of  $\text{H}_2\text{O}$  calculated using the stationary (UKRmol+) and time-dependent (RMT) approaches, shown in comparison with experimental data from Katayama *et al.* [63], Haddad and Samson [65] and photoabsorption calculations from Ruberti *et al.* [66] and Tenorio *et al.* [67] and photoionization calculation of Modak and Antony [61]. (a) Time-independent calculation with the larger model; both smoothed and raw UKRmol+ are shown. (b) RMT and UKRmol+ results for the smaller model compared with the larger model results.

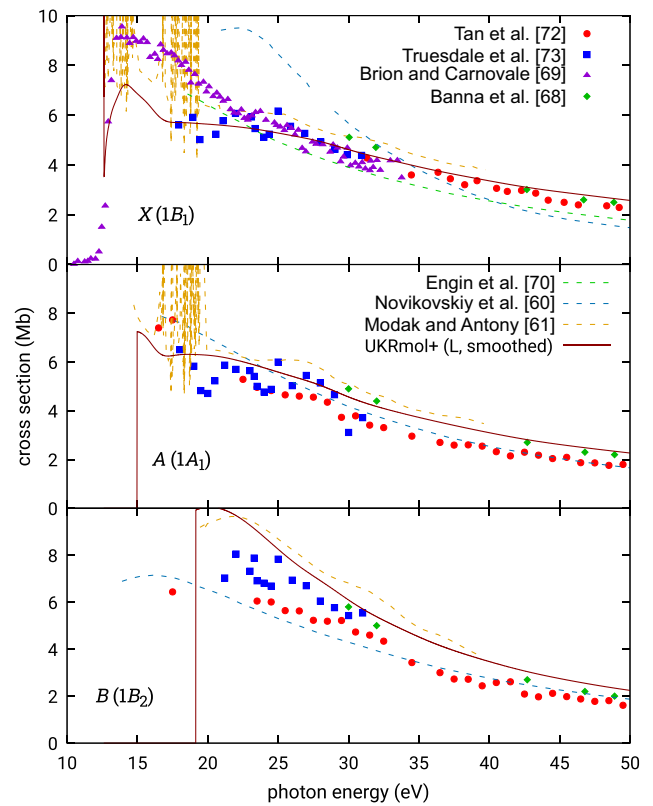


FIG. 5. Partial orientation-averaged cross sections for one-photon photoionization of  $\text{H}_2\text{O}$  calculated using the stationary (UKRmol+) approach. The transitions to the three lowest states of  $\text{H}_2\text{O}^+$  are shown. Experimental data are from Tan *et al.* [72], Truesdale *et al.* [73], Brion and Carnovale [69], and Banna *et al.* [68] and calculations are from Engin *et al.* [70], Novikovskiy *et al.* [60], and Modak and Antony [61]. The UKRmol+ results for energies smaller than 20 eV are heavily influenced by smoothing.

For the time-dependent calculation we used long pulses (around 30 cycles), linearly polarized along one of the three coordinate axes, and intensity  $I = 10^{10}$  W/cm<sup>2</sup>. The pseudo-stationary orientation-averaged photoionization cross section was obtained from Eq. (20), where  $\kappa$  is the calculated ionization rate averaged over the three orthogonal polarization directions.

## B. Single-photon ionization

Figure 4 presents a benchmark RMT calculation for the total stationary photoionization cross sections, as well as time-independent UKRmol+ results. Figure 4(a) shows the latter results for the bigger model compared with earlier experiments and calculations. Figure 4(b) shows both time-dependent and -independent calculations with the smaller model.

When the larger model is used, the UKRmol+ calculation reproduces the experimental data for the total cross section very closely, down to a very low broad bump between 25 and 30 eV, which there appears to be a cumulative effect of the Rydberg resonances in that area. This calculation also reproduces well the partial cross sections for ionization into the lowest three states of  $\text{H}_2\text{O}^+$  shown in Fig. 5. In this case,

our cross sections tend to be larger than the older experimental data, but generally very close to the most recent measurement by Banna *et al.* [68]. The exception is the photoionization into the ground state of  $\text{H}_2\text{O}^+$ , for which the experimental results of Brion and Carnovale [69] are noticeably bigger than our results below 20 eV. Note, however, that in this energy range our results are strongly influenced by the smoothing procedure (discussed below).

For the photoionization into the ground state of  $\text{H}_2\text{O}^+$ , Fig. 5 includes the results of Engin *et al.* [70] obtained from a fixed-nuclei density-functional-theory calculation that shows slightly poorer agreement with the experiment. However, very recent *B*-spline density-functional-theory calculations [71] show similarly good agreement to ours, whereas earlier *R*-matrix results [61] show poorer agreement particularly for higher photon energies (their calculations go up to 40 eV only). This calculation employed a smaller active space, fewer cationic states in Eq. (19), did not use *B*-splines (which ensure a significantly improved description of the continuum), and also only included continuum partial waves up to  $\ell = 4$ . Finally, the single-center calculations of Novikovskiy *et al.* [60] seem to show better agreement with experiment at higher energies for the second and third states of  $\text{H}_2\text{O}^+$ . In contrast to photoionization calculations for  $\text{CO}_2$  [37] and  $\text{NO}_2$  [36], partial waves beyond  $\ell = 4$  do not contribute significantly to photoionization of water at energies below 50 eV, most likely due to the location of the oxygen atom with *p*-type valence orbitals close to the center of mass; *s* and *d* partial waves then constitute the dominant contribution to photoionization into the low-lying valence states of  $\text{H}_2\text{O}^+$ .

We note that only the partial cross sections for the lowest 14 final ionic states were used to produce the time-independent total cross section for the larger model in Fig. 4. Those for the cationic states with thresholds greater than 33 eV were not, as they showed (particularly that for state 15) an unusual energy dependence that led us to believe there may be a problem with accurate description of at least some of these states (inclusion of all states, excluding 15, leads to small changes to the size of the cross section that slightly improve agreement with experiment).

The curves labeled smoothed were produced from partial-wave dipoles convoluted with a Gaussian distribution with the width dependent on the photoelectron kinetic energy (around 3 meV close to the channel threshold, linearly increasing to around 3 eV at the high-energy end of the energy range), as implemented in the program DIPELM [30]. The aim of the smoothing is to remove the very narrow spikes associated with resonances that are unlikely to be visible in the experiment. As can be seen in Fig. 4(a), both raw and smoothed cross sections agree very well with experiment above around 18 eV. Below that energy, the raw cross section is dominated by the Rydberg series converging to the second and third ionization thresholds. When smoothed, the cross section in this region shows clearly a nonphysical energy dependence: On the one hand, the sharp steplike character will, in reality, be smoothed by the vibrational motion; on the other hand, some effect due to the closely spaced resonances might be visible in the physical cross section.

Figure 4(b) shows the comparison between the RMT results and the one-photon time-independent results from

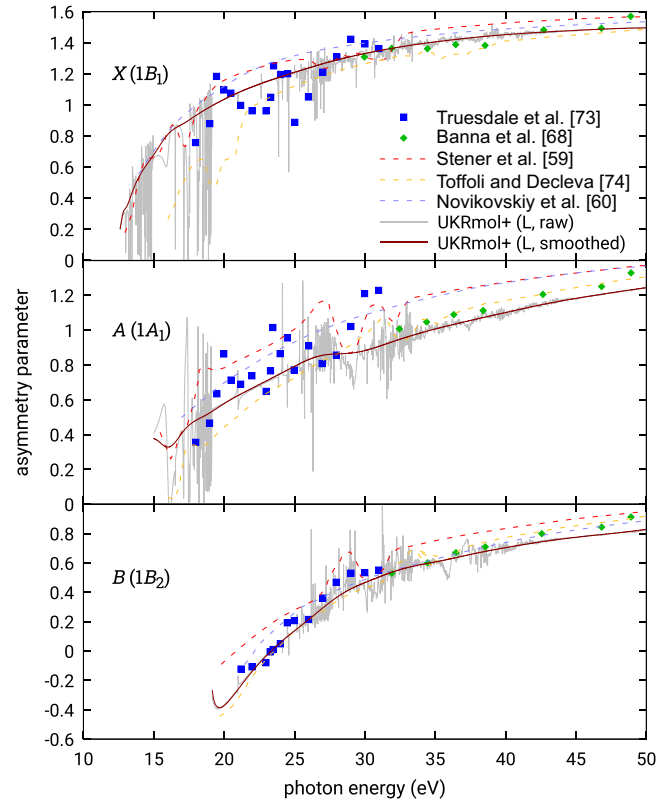


FIG. 6. Asymmetry parameter for one-photon ionization of  $\text{H}_2\text{O}$  into the first three ionic states as calculated in UKRmol+. The experiments of Truesdale *et al.* [73] and Banna *et al.* [68] and calculations of Stener *et al.* [59], Toffoli and Decleva [74], and Novikovskiy *et al.* [60] are also shown.

UKRmol+, both determined using the smaller model. Use of this model leads to a bigger cross section in most of the energy range presented: The difference is mainly due to the change of active space with a significantly smaller effect linked to the different number of states included in Eq. (19). The agreement between the UKRmol+ and RMT data confirms the validity of the time-dependent method for polyatomic molecules in the perturbative limit of weak and long pulses.

Finally, in Fig. 6 we show the UKRmol+ asymmetry parameters for the *X*, *A*, and *B* states in comparison to available theoretical and experimental data. The *R*-matrix results are in excellent agreement with the experiment of Banna *et al.* [68] at higher energies above approximately 30 eV. At low energies the experimental data of Truesdale *et al.* [73] exhibit a large scatter in the region of intense autoionizing resonances. Nevertheless, our smoothed results interpolate the experimental data very well, especially for the *B* state, where the scatter in the experimental data is smaller. Other calculations deviate from the experiment noticeably in either the high- or the low-energy range.

### C. Strong-field ionization: Polarization-dependent photoionization yields

To assess the accuracy of simulation of short and strong laser-driven processes in polyatomic molecules, we attempted to reproduce the results from single-active-electron



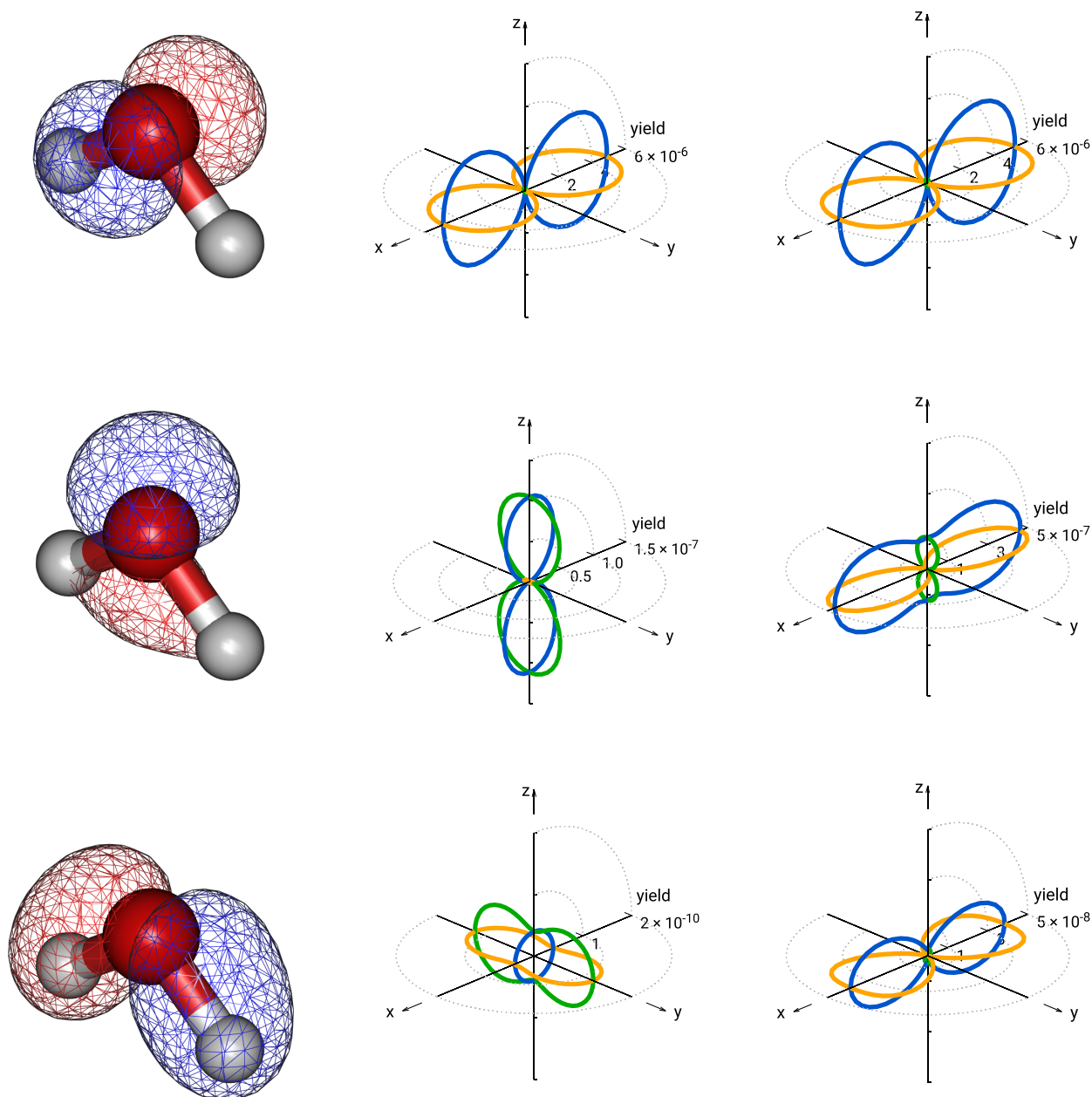


FIG. 7. Dimensionless strong-field ionization yield associated with the ionization of water to (from top to bottom) the  $X\ 1^2B_1$ ,  $A\ 1^2A_1$ , and  $B\ 1^2B_2$  states of  $H_2O^+$ . The left column shows visualization of the Hartree-Fock (Dyson) orbitals from which the electron is ionized ( $1b_1$ ,  $3a_1$ , and  $1b_2$ , respectively) from GABEDIT [75]. The middle column shows polarization-orientation-dependent yields using the single-channel model (A, corresponding to ionization of a single orbital of  $H_2O$ ). The right column is the same as the middle but with the electronic coupling between cation states included (model B). Different colors are used for different coordinate planes for easier identification. Note the different scales in the plots of the middle and right-hand columns.

calculations of Petretti *et al.* [54], where it was suggested that the total yield of electrons ionized from a particular state of  $H_2O$  by a linearly polarized pulse depends on the polarization direction in a way that follows the shape of the ionized orbital. Our results for these yields are shown in Fig. 7. Two different models have been used for this calculation.

(A) *Single-channel Hartree-Fock model.* The ionization can result in only one specific ionic state; three separate calculations are run in which only one of the three lowest-lying ionic states ( $1^2B_1$ ,  $1^2A_1$ , or  $1^2B_2$ ) is included in the wave function of the  $(N + 1)$ -electron system (19).

(B) *Coupled model.* Any of the considered final ionic states can be produced; a single calculation is run, which includes all three lowest electronic states of  $H_2O^+$ , fully coupled.

In both cases we used the basis cc-pVTZ, with one frozen and four active orbitals (chosen to resemble the model used in [54]),  $a = 15$  a.u., partial waves up to  $\ell = 4$ , and a purely  $B$ -spline continuum consisting of 15  $B$ -splines of order 6. Unlike the benchmark calculations in the preceding section, we used Hartree-Fock orbitals of the *neutral* molecule, in order to capture the neutral molecule structure reasonably well even in this very crude model. The resulting vertical

TABLE III. Vertical ionization potentials for H<sub>2</sub>O: calculated vs manually shifted.

Final state	$V^{ion}$ (model A)	$V^{ion}$ (model B)
$X\ 1^2B_1$	13.79 → 13.15 eV	13.83 → 13.15 eV
$A\ 1^2A_1$	15.78 → 15.09 eV	15.83 → 15.15 eV
$B\ 1^2B_2$	19.37 → 18.69 eV	19.41 → 18.73 eV

ionization thresholds are summarized in Table III. In the actual calculation in RMT the ground-state energy was shifted so that all thresholds from [54] or the lowest one were recovered for models A and B, respectively. This is important, because in the nonperturbative regime the yields are exponentially sensitive to the threshold energy; our calculated ionic energies are inaccurate because of the use of the same few molecular orbitals for both the charged and the neutral molecule. Note that with the chosen active space, while states  $X$  and  $B$  are single-configuration states, state  $A$  is formed by two configurations; however, we have confirmed that the contribution of the higher-energy configuration is negligible. In Table IV we give the permanent and transition dipole elements for the three states as calculated in our model and we discuss them further below.

To generate Figs. 7 and 8 we used a linearly polarized eight-cycle  $\sin^2$  pulse with the wavelength  $\lambda = 800$  nm and intensity  $I = 20$  TW/cm<sup>2</sup> with many different orientations of the polarization vector. After 2000 a.u. (49.8 fs) of time of the simulation [around 1150 a.u. (28.6 fs) after the end of

TABLE IV. Permanent and transition dipoles (in atomic units) for the three states of H<sub>2</sub>O<sup>+</sup> included in the coupled model B. The dipole component is also indicated. For the orientation of the molecule used in this work see Fig. 7.

	$X\ 1^2B_1$	$A\ 1^2A_1$	$B\ 1^2B_2$
$X\ 1^2B_1$	$0.737\ \hat{z}$	$0.147\ \hat{x}$	
$A\ 1^2A_1$	$0.147\ \hat{x}$	$0.595\ \hat{z}$	$0.161\ \hat{y}$
$B\ 1^2B_2$		$0.161\ \hat{y}$	$1.076\ \hat{z}$

the pulse] we obtained the ionization yield by integrating the electron density for distances  $r > 65$  a.u. By omitting contributions from the density closer to the origin than  $r = 65$  a.u. we avoided counting towards the ionization yield the electron density related to excited bound states and included only the outgoing wave packet.

With model A we get qualitative agreement with the findings of Petretti *et al.* [54], as can be seen comparing the middle column of Fig. 7 with the data presented by Petretti *et al.* in their Fig. 2 and looking also at Fig. 8. (The latter figure presents the same data as Fig. 7, this time focused on a particular coordinate plane and explicitly includes the results from [54].) That is, the yield from the photoionization of a single orbital is maximal when the polarization of the field is aligned with the orientation of the orbital and it quickly decreases with angular deviation. A quantitative agreement with said calculation cannot be expected, due to the differences in both the molecular and ionization descriptions and the

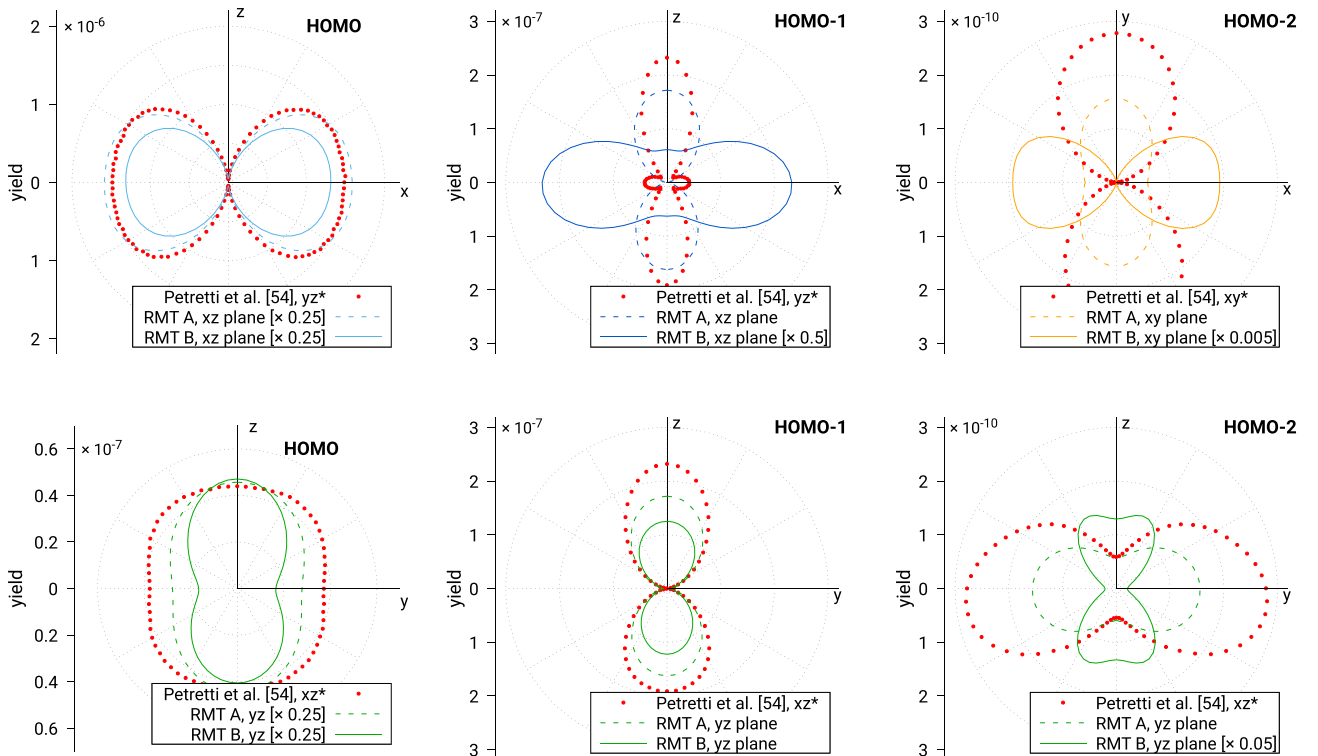


FIG. 8. Detailed comparison of slices of the ionization yields presented in Fig. 7 for our two models and with the results from [54]. The color of the lines is consistent with that of Fig. 7. The RMT calculation with model A qualitatively agrees with the earlier results. Note that in [54] the molecule was placed in the  $xz$  plane with  $z_{H_1} = z_{H_2} > z_O$ , while in the present calculation the  $yz$  plane was used, with  $z_{H_1} = z_{H_2} < z_O$ . All results from [54] are thus transformed to the coordinate system used in this work.

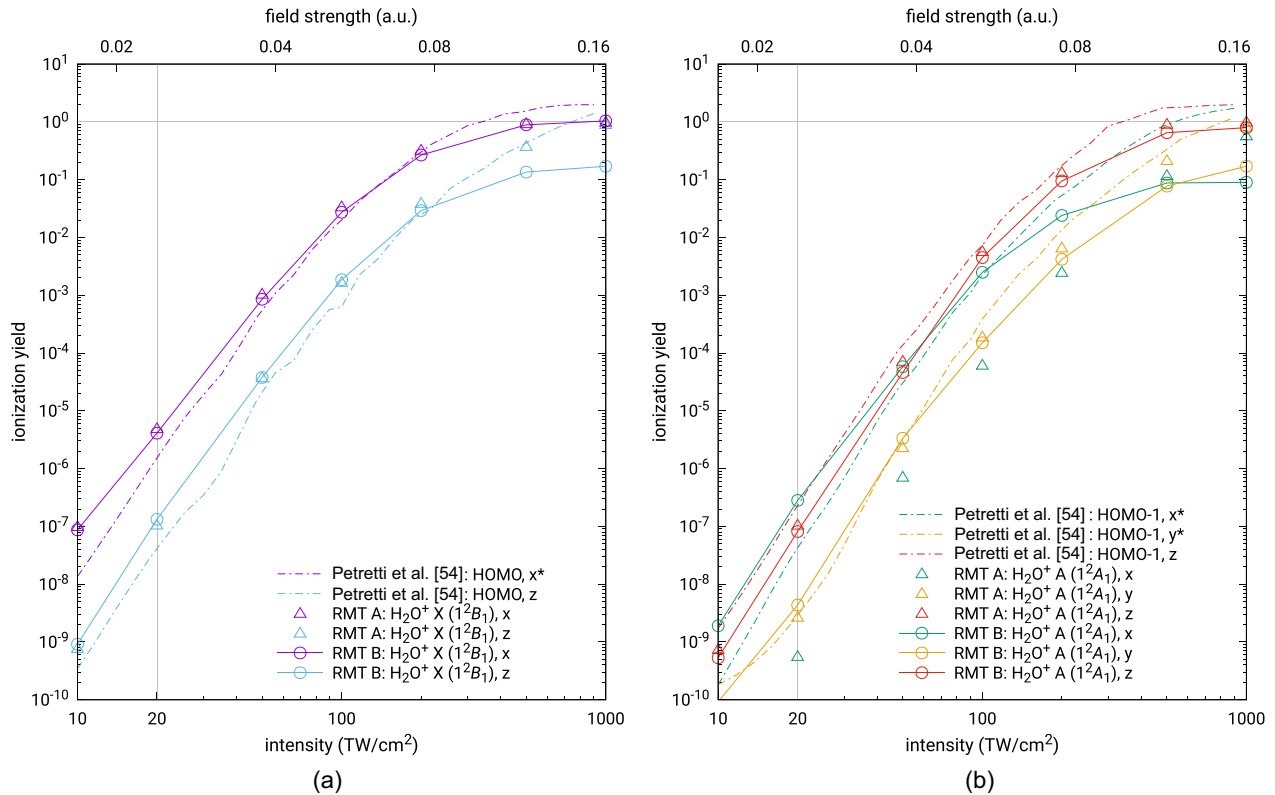


FIG. 9. Peak field intensity dependence of the yield pertaining to the selected pulse polarization for the two lowest final states (a)  $X (1^2B_1)$  and (b)  $A (1^2A_1)$  of the  $H_2O^+$  cation, compared to the results of Petretti *et al.* [54]. The RMT results using the uncoupled model A are indicated with open triangles, while those from the coupled model B are indicated by solid lines with open circles. Note that the maximal total yields in Fig. 9 calculated by Petretti *et al.* [54] go to 2 in the limit of large intensities due to an additional factor of 2 used to correct the yields in the low intensities; this factor is said by the authors to be surplus for large intensities. In contrast, the maximal total yields calculated from RMT have the limit of 1, corresponding to a complete ionization of the single ionizable electron available to the theory. This limit is reached also in the case of the coupled-state calculations when the yields are summed over all final states.

different analysis techniques used to determine the ionization yields.

For model B, the states are coupled, as is the case physically. Here the final distribution of the yield always resembles the highest occupied molecular orbital (HOMO)  $1b_1$ , regardless of the chosen final residual ion state. This is because the ionization of the deeper-lying states (orbitals) is exponentially suppressed and state coupling (both field and correlation driven) is responsible for redistribution of the dominant photoelectron yield from the state  $X (1^2B_1)$  to the deeper-lying channels  $A (1^2A_1)$  and  $B (1^2B_2)$ . The only non-negligible exception is the ionization into the  $A$  state by a pulse with field polarization along the molecular axis (second row, right-hand column in Fig. 7), where the direct ionization of the  $A$  state (HOMO-1) is still visible in the overall polarization dependence of the ionization yield. This is mainly due to the orthogonality of the nodal planes of the  $p$ -type HOMO and HOMO-1 for oxygen. This allows the HOMO-1 to show when the polarization vector lies in the nodal plane of the otherwise dominant HOMO.

Crucially, our results show that the exponential scaling of ionization yields is significantly mitigated when coupling between the states is allowed. We can see that the coupled-channel yields decrease always by an order of magnitude as we go from state  $X$  to  $A$  and  $B$ , while in the uncoupled model

the yield of state  $B$  is three orders of magnitude smaller than the yield of state  $A$ . Therefore, our results demonstrate the key importance of channel coupling in strong-field ionization of molecules, just as we have found previously for atomic systems [76,77].

Interestingly, the picture changes for the coupled model when even larger intensities are used (see Fig. 9). While at the investigated intensity of 20 TW/cm<sup>2</sup> the maximal yield corresponding to the final state  $A (1^2A_1)$  is reached with pulses polarized along the  $x$  axis, at intensities of 100 TW/cm<sup>2</sup> and higher the total yield corresponding to this state is maximal for polarization along the  $z$  axis instead. Thus, for very high intensities, the yield distribution in the coupled model mimics the uncoupled case. Nevertheless, quantitative differences between the coupled and uncoupled models prevail even at these high intensities. Therefore, our calculations reveal two different effects: (a) the importance of a coupled-channel approach (electron correlation) and (b) the switching of the relative importance of ionization yields for the different polarizations.

Effect (b) might be related to the transition from the below-barrier to above-barrier ionization regime [17]. A rough estimate for a purely static field places the intensity dividing these two regions at 110–220 TW/cm<sup>2</sup>, which lies in the vicinity of the observed crossing point of approximately 50 TW/cm<sup>2</sup>.

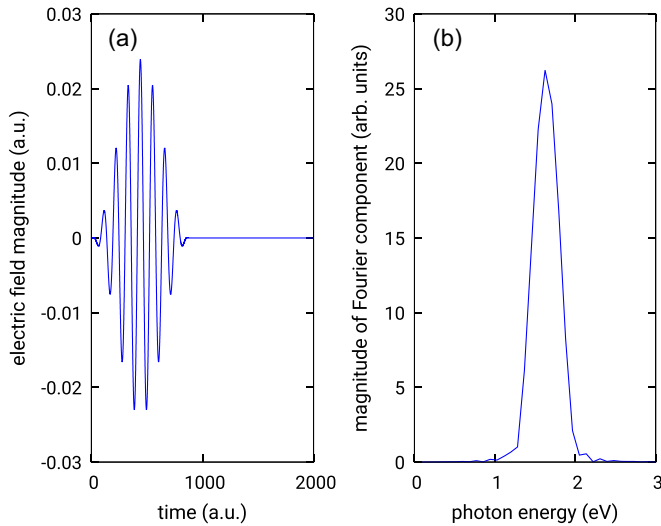


FIG. 10. (a) Time dependence of the electric-field amplitude used in strong-field ionization of  $\text{H}_2\text{O}$  and (b) its spectrum.

More insight into effect (a), the coupled-channel dynamics, can be gained with the help of the transition dipole moments, shown in Table IV, in combination with the vertical excitation energies of the states shown in Table III and the photon spectrum of the pulse shown in Fig. 10. We see that the  $X \rightarrow A$  transition can be realized by absorption of the photon by the ion. In fact, the 2-eV transition  $X \rightarrow A$  is close to resonance with the dominant spectral component of the field peaking at approximately 1.6 eV (see Fig. 10). However, the  $B$  state cannot be reached by successive absorptions of linearly polarized photons since the  $X \rightarrow A$  and  $A \rightarrow B$  transitions are orthogonal to each other. The enhancement of ionization into state  $B$  therefore suggests that electron correlation contributes non-negligibly too.

Indeed, we were able to confirm that removing the dipolar couplings  $W^D$  between the ionic states (the off-diagonal terms in Table IV), responsible for channel couplings due to photon absorption by the residual ion, does not change the results noticeably, therefore corroborating the importance of field-free and/or laser-assisted electron correlation. The importance of the laser-induced transitions in the ion is the only interaction we can straightforwardly test in the current Hartree-Fock model where both the ionic and the neutral states are described by a single configuration: This interaction can be consistently switched off in both the inner and the outer regions. Studying the relative importance of the  $W^P$  (laser-assisted) and field-free electron correlations would require nontrivial manipulations of many intermediate quantities, which goes beyond the remit of this work but may be done in the future. We remark that the type of electron-correlation accompanying the laser-assisted one corresponds to the field-free electron-impact electronic excitation. The importance of this interaction is supported by the fact that electron-impact electronically inelastic cross sections are typically larger than the single-photon cross sections. Previous analytic works [4,5] have also highlighted the key importance of electron correlation in obtaining accurate ionization yields in small molecules.

Finally, we remark that similar trends concerning the importance of electron correlation and its dependence on field strength were reported in static field calculations [17] for strong-field ionization of water. There it was found that electron correlation enhances significantly the total photoelectron yield and that this effect becomes less important as the field strength is increased from 0.05 a.u. to 0.14 a.u. This general conclusion is in agreement with our calculations which show greater differences between the coupled and uncoupled models at low-field intensities. Additionally, our calculations for a time-dependent field predict a change in the relative importance of the yields for state  $A$  for the different polarizations of the field as shown in Fig. 9 and discussed above.

## V. CONCLUSION

We have demonstrated that the  $R$ -matrix with time method is able to describe many-electron and multiphoton processes in molecules interacting with laser fields. This was illustrated for weak-field two-photon ionization of  $\text{H}_2$  and one-photon and strong-field ionization of  $\text{H}_2\text{O}$  using coupled-channel models. The calculated photoionization cross sections are in excellent agreement with experiment and prior accurate calculations. Our strong-field calculations for  $\text{H}_2\text{O}$  show that when state coupling is included the exponential penalty of tunnel ionization is removed, in agreement with earlier analytical analysis [4,5], highlighting the importance of using multielectron approaches to strong-field molecular dynamics.

We show in these model calculations that the accuracy of the time-dependent results is inherently limited by the time-independent structural data supplied as input: For two-photon ionization of the hydrogen molecule, the cross-section values eventually converged to the time-independent ones when the spectral bandwidth related to the sharp turn-on of the field was narrowed, but did not improve beyond the time-independent results. For one-photon ionization of water, the accuracy of the cross sections was similarly limited by the active space used for generating the molecular data.

In the case of the water molecule we were able to confirm that, in the single-channel approximation and at intensity of  $20 \text{ TW}/\text{cm}^2$ , the polarization-orientation-dependent ionization yield associated with a given final ionic state of the molecule follows the shape of the corresponding orbital. However, we have shown that the picture completely changes when channel coupling is included; then, due to the tunneling exponential law and state coupling, ionization into state  $X$  completely dominates and the electron angular distribution predominantly resembles the HOMO, independently of the final ionic state. Our intensity-dependent calculations show that the picture reverses again at high intensities beyond approximately  $100 \text{ TW}/\text{cm}^2$  where the coupled-channel yields resemble the uncoupled results. Nevertheless, inclusion of the channel coupling in both cases affects the magnitudes of the yields significantly and therefore cannot be omitted.

In our calculations the role of field-free state coupling and electron correlation is intertwined with the laser-induced electronic dynamics and cannot be directly separated but can be inferred indirectly by varying the laser-field parameters, in particular, the wavelength and duration. Future work will therefore focus on detailed investigation of the role of

electron correlation in strong-field ionization of small molecules using different correlation models and employing pulses of various parameters, in particular mid-IR pulses whose use has proved instrumental in revealing the significant role of electron correlation in strong-field ionization [7] and high harmonic generation [3,52] of CO<sub>2</sub>.

The generality of the RMT approach and its link to the UKRmol+ package makes it possible, as well as reasonably straightforward, to treat any molecule with RMT: from diatomics to fairly large polyatomic molecules of biological interest. The current limitation is computational: Due to the lower molecular symmetry, performing calculations on the same level of quality as for atoms remains a challenge. However, the use of UKRmol+ and RMT enables great flexibility in terms of the molecular models that can be employed. Simple single-channel Hartree Fock models and coupled-state descriptions that include electron correlation are similarly straightforward to set up. This means that appropriate models can be found to study in detail a variety of targets and ultrafast processes within the fixed-nuclei approximation.

All data generated for this publication can be accessed at The Open University's research repository [78] and used under CC BY-NC 4.0 license.

## ACKNOWLEDGMENTS

Both the RMT code and UKRmol+ suites are part of the UK-AMOR suite and can be accessed for free from Ref. [79]. The work presented in this paper was supported by EPSRC under Grants No. EP/P022146/1 and No. EP/P013953/1. Access to the ARCHER UK National Supercomputing Service [80] was obtained via the UK-AMOR consortium funded by EPSRC (Grant No. EP/R029342/1). Some computational resources were supplied by the project “e-Infrastruktura CZ” (Project No. e-INFRA LM2018140) provided within the program Projects of Large Research, Development and Innovations Infrastructures. This work was also supported by The Ministry of Education, Youth and Sports of the Czech Republic from the Large Infrastructures for Research, Experimental Development and Innovations project “IT4Innovations National Supercomputing Center,” Project No. LM2015070. The development of RMT and UKRmol+ has benefited from computational support from the Computational Science Centre for Research Communities, through CCPQ. Z.M. acknowledges funding from the PRIMUS program of the Charles University (Grant No. PRIMUS/20/SCI/003). Z.M. and J.B. acknowledge support from the Czech Science Foundation through Project No. GA CR 20-15548Y.

- 
- [1] M. Nisoli, P. Decleva, F. Calegari, A. Palacios, and F. Martín, *Chem. Rev.* **117**, 10760 (2017).
- [2] A. J. Uzan, H. Soifer, O. Pedatzur, A. Clergerie, S. Larroque, B. D. Bruner, B. Pons, M. Ivanov, O. Smirnova, and N. Dudovich, *Nat. Photon.* **14**, 188 (2020).
- [3] B. D. Bruner, Z. Mašín, M. Negro, F. Morales, D. Brambila, M. Devetta, D. Faccialà, A. G. Harvey, M. Ivanov, Y. Mairesse, S. Patchkovskii, V. Serbinenko, H. Soifer, S. Stagira, C. Vozzi, N. Dudovich, and O. Smirnova, *Faraday Discuss.* **194**, 369 (2016).
- [4] Z. B. Walters and O. Smirnova, *J. Phys. B* **43**, 161002 (2010).
- [5] L. Torlina, M. Ivanov, Z. B. Walters, and O. Smirnova, *Phys. Rev. A* **86**, 043409 (2012).
- [6] V. P. Majety, A. Zielinski, and A. Scrinzi, *New J. Phys.* **17**, 063002 (2015).
- [7] V. P. Majety and A. Scrinzi, *Phys. Rev. A* **96**, 053421 (2017).
- [8] M. Ruberti, *J. Chem. Theory Comput.* **15**, 3635 (2019).
- [9] M. Spanner and S. Patchkovskii, *Phys. Rev. A* **80**, 063411 (2009).
- [10] S. Patchkovskii and M. S. Schuurman, *Phys. Rev. A* **96**, 053405 (2017).
- [11] C. Marante, M. Klinker, I. Corral, J. González-Vázquez, L. Argenti, and F. Martín, *J. Chem. Theory Comput.* **13**, 499 (2017).
- [12] T. Sato and K. L. Ishikawa, *Phys. Rev. A* **91**, 023417 (2015).
- [13] J. Zanghellini, M. Kitzler, Z. Zhang, and T. Brabec, *J. Mod. Opt.* **52**, 479 (2005).
- [14] E. Lötstedt, T. Kato, and K. Yamanouchi, in *Progress in Ultrafast Intense Laser Science XIII*, edited by K. Yamanouchi, W. T. Hill III, and G. G. Paulus (Springer International, Cham, 2017), pp. 15–40.
- [15] T. Sato, H. Pathak, Y. Orimo, and K. L. Ishikawa, *J. Chem. Phys.* **148**, 051101 (2018).
- [16] H. Pathak, T. Sato, and K. L. Ishikawa, *J. Chem. Phys.* **152**, 124115 (2020).
- [17] T.-C. Jagau, *J. Chem. Phys.* **148**, 204102 (2018).
- [18] J. Colgan and M. S. Pindzola, *Eur. Phys. J. D* **66**, 284 (2012).
- [19] K. L. Ishikawa and T. Sato, *IEEE J. Sel. Top. Quantum Electron.* **21**, 1 (2015).
- [20] L. R. Moore, M. A. Lysaght, L. A. A. Nikolopoulos, J. S. Parker, H. W. van der Hart, and K. T. Taylor, *J. Mod. Opt.* **58**, 1132 (2011).
- [21] L. A. A. Nikolopoulos, J. S. Parker, and K. T. Taylor, *Phys. Rev. A* **78**, 063420 (2008).
- [22] A. C. Brown and H. W. van der Hart, *Phys. Rev. Lett.* **117**, 093201 (2016).
- [23] D. D. A. Clarke, G. S. J. Armstrong, A. C. Brown, and H. W. van der Hart, *Phys. Rev. A* **98**, 053442 (2018).
- [24] G. S. J. Armstrong, D. D. A. Clarke, J. Benda, J. Wragg, A. C. Brown, and H. W. van der Hart, *Phys. Rev. A* **100**, 063416 (2019).
- [25] G. S. J. Armstrong, D. D. A. Clarke, J. Benda, A. C. Brown, and H. W. van der Hart, *Phys. Rev. A* **101**, 041401(R) (2020).
- [26] J. Wragg, D. D. A. Clarke, G. S. J. Armstrong, A. C. Brown, C. P. Ballance, and H. W. van der Hart, *Phys. Rev. Lett.* **123**, 163001 (2019).
- [27] C. Ó Broin and L. A. A. Nikolopoulos, *Phys. Rev. A* **92**, 063428 (2015).
- [28] A. C. Brown, G. S. J. Armstrong, J. Benda, D. D. A. Clarke, J. Wragg, K. Hamilton, Z. Mašín, J. D. Gorfinkiel, and H. van der Hart, *Comput. Phys. Commun.* **250**, 107062 (2020).
- [29] P. G. Burke, *R-Matrix Theory of Atomic Collisions* (Springer, Berlin, 2011).
- [30] Z. Mašín, J. Benda, J. D. Gorfinkiel, A. G. Harvey, and J. Tennyson, *Comput. Phys. Commun.* **249**, 107092 (2020).

- [31] J. M. Carr, P. G. Galiatsatos, J. D. Gorfinkiel, A. G. Harvey, M. A. Lysaght, D. Madden, Z. Mašín, M. Plummer, J. Tennyson, and H. N. Varambhia, *Eur. Phys. J. D* **66**, 58 (2012).
- [32] J. Tennyson, *Phys. Rep.* **491**, 29 (2010).
- [33] J. D. Gorfinkiel and S. Ptasinska, *J. Phys. B* **50**, 182001 (2017).
- [34] A. G. Harvey, D. S. Brambilla, F. Morales, and D. Smirnova, *J. Phys. B* **47**, 215005 (2014).
- [35] D. S. Brambilla, A. G. Harvey, Z. Mašín, J. D. Gorfinkiel, and O. Smirnova, *J. Phys. B* **48**, 245101 (2015).
- [36] D. S. Brambilla, A. G. Harvey, K. Houfek, Z. Mašín, and O. Smirnova, *Phys. Chem. Chem. Phys.* **19**, 19673 (2017).
- [37] Z. Mašín, A. G. Harvey, M. Spanner, S. Patchkovskii, M. Ivanov, and O. Smirnova, *J. Phys. B* **51**, 134006 (2018).
- [38] D. R. Austin, F. McGrath, L. Miseikis, D. Wood, P. Hawkins, A. S. Johnson, M. Vacher, Z. Mašín, A. Harvey, M. Ivanov, O. Smirnova, and J. P. Marangos, *Faraday Discuss.* **194**, 349 (2016).
- [39] H.-J. Werner, P. J. Knowles, G. Knizia, F. R. Manby, and M. Schütz, *WIREs Comput. Mol. Sci.* **2**, 242 (2012).
- [40] H. Ibrahim, C. Lefebvre, A. D. Brandrauk, A. Staudte, and F. Légaré, *J. Phys. B* **51**, 042002 (2018).
- [41] J. Colgan, D. H. Glass, K. Higgins, and P. G. Burke, *J. Phys. B* **34**, 2089 (2001).
- [42] A. Apalategui and A. Saenz, *J. Phys. B* **35**, 1909 (2002).
- [43] A. M. Machado and M. Masili, *J. Chem. Phys.* **120**, 7505 (2004).
- [44] F. Morales, F. Martín, D. A. Horner, T. N. Rescigno, and C. W. McCurdy, *J. Phys. B* **42**, 134013 (2009).
- [45] D. G. A. Smith, L. A. Burns, A. C. Simmonett, R. M. Parrish, M. C. Schieber, R. Galvelis, P. Kraus, H. Kruse, R. Di Remigio, A. Alenaizan *et al.*, *J. Chem. Phys.* **152**, 184108 (2020).
- [46] H. Nakashima and H. Nakatsuji, *J. Chem. Phys.* **149**, 244116 (2018).
- [47] G. V. Marr, R. M. Holmes, and K. Codling, *J. Phys. B* **13**, 283 (1980).
- [48] S. Southworth, W. D. Brewer, C. M. Truesdale, P. H. Kobrin, D. W. Lindle, and D. A. Shirley, *J. Electron Spectrosc.* **26**, 43 (1982).
- [49] A. C. Parr, J. E. Hardis, S. H. Southworth, C. S. Feigerle, T. A. Ferrett, D. M. P. Holland, F. M. Quinn, B. R. Dobson, J. B. West, G. V. Marr, and J. L. Dehmer, *Phys. Rev. A* **37**, 437 (1988).
- [50] B. Zimmermann, V. McKoy, S. H. Southworth, E. P. Kanter, B. Krässig, and R. Wehlitz, *Phys. Rev. A* **91**, 053410 (2015).
- [51] J. Tennyson, C. J. Noble, and P. G. Burke, *Int. J. Quantum Chem.* **29**, 1033 (1986).
- [52] M. Ruberti, P. Decleva, and V. Averbukh, *Phys. Chem. Chem. Phys.* **20**, 8311 (2018).
- [53] M. Ruberti, *Phys. Chem. Chem. Phys.* **21**, 17584 (2019).
- [54] S. Petretti, A. Saenz, A. Castro, and P. Decleva, *Chem. Phys.* **414**, 45 (2013).
- [55] A. Galstyan, Y. V. Popov, N. Janssens, F. Mota-Furtado, P. F. O'Mahony, P. Decleva, N. Quadri, O. Chuluunbaatar, and B. Piraux, *Chem. Phys.* **504**, 22 (2018).
- [56] Z. Chen and F. He, *J. Opt. Soc. Am. B* **36**, 2571 (2019).
- [57] P. Hoerner and H. B. Schlegel, *J. Phys. Chem. A* **121**, 1336 (2017).
- [58] I. Cacelli, V. Carravetta, and R. Moccia, *J. Chem. Phys.* **97**, 320 (1992).
- [59] M. Stener, G. Fronzoni, D. Toffoli, and P. Decleva, *Chem. Phys.* **282**, 337 (2002).
- [60] N. M. Novikovskiy, V. L. Sukhorukov, A. N. Artemyev, and P. V. Demekhin, *Eur. Phys. J. D* **73**, 79 (2019).
- [61] P. Modak and B. Antony, *J. Phys. B* **53**, 045202 (2020).
- [62] A. W. Potts and W. C. Price, *Proc. R. Soc. London Ser. A* **326**, 181 (1972).
- [63] D. H. Katayama, R. E. Huffman, and C. L. O'Bryan, *J. Chem. Phys.* **59**, 4309 (1973).
- [64] C. R. Brundle, D. W. Turner, and W. C. Price, *Proc. R. Soc. London Ser. A* **307**, 27 (1968).
- [65] G. N. Haddad and J. A. R. Samson, *J. Chem. Phys.* **84**, 6623 (1986).
- [66] M. Ruberti, R. Yun, K. Gokhberg, S. Kopelke, L. S. Cederbaum, F. Tarantelli, and V. Averbukh, *J. Chem. Phys.* **139**, 144107 (2013).
- [67] B. N. C. Tenorio, M. A. C. Nascimento, S. Coriani, and A. B. Rocha, *J. Chem. Theory Comput.* **12**, 4440 (2016).
- [68] M. S. Banna, B. H. McQuaide, R. Malutzki, and V. Schmidt, *J. Chem. Phys.* **84**, 4739 (1986).
- [69] C. E. Brion and F. Carnovale, *Chem. Phys.* **100**, 291 (1985).
- [70] S. Engin, J. González-Vázquez, G. G. Maliyar, A. R. Milosavljević, T. Ono, S. Nandi, D. Iablonski, K. Kooser, J. D. Bozek, P. Decleva, E. Kukuk, K. Ueda, and F. Martín, *Struct. Dyn.* **6**, 054101 (2019).
- [71] T. Moitra, A. Ponzi, H. Koch, S. Coriani, and P. Decleva, *J. Phys. Chem. Lett.* **11**, 5330 (2020).
- [72] K. H. Tan, C. E. Brion, P. E. van der Leeuw, and M. J. van der Wiel, *Chem. Phys.* **29**, 299 (1978).
- [73] C. M. Truesdale, S. Southworth, P. H. Kobrin, and D. W. Lindle, *J. Chem. Phys.* **76**, 860 (1982).
- [74] D. Toffoli and P. Decleva, *J. Chem. Theory Comput.* **12**, 4996 (2016).
- [75] A.-R. Allouche, *J. Comput. Chem.* **32**, 174 (2011).
- [76] A. C. Brown and H. W. van der Hart, *Phys. Rev. A* **86**, 063416 (2012).
- [77] O. Hassounch, A. C. Brown, and H. W. van der Hart, *Phys. Rev. A* **89**, 033409 (2014).
- [78] [https://ordo.open.ac.uk/articles/dataset/Perturbative\\_and\\_non-perturbative\\_photoionization\\_of\\_H2\\_and\\_H2O\\_using\\_RMT/12199011](https://ordo.open.ac.uk/articles/dataset/Perturbative_and_non-perturbative_photoionization_of_H2_and_H2O_using_RMT/12199011) (DOI:10.21954/ou.rd.12199011.v2).
- [79] The UK-AMOR consortium, <https://www.ukamor.com/#/software> (2019).
- [80] [www.archer.ac.uk](http://www.archer.ac.uk).

*Correction:* The previously published Figure 8 was processed improperly during production, causing some dashed lines to appear as solid lines. The figure has now been replaced.